Magnetic configuration effects on the

Wendelstein 7-X stellarator

A. Dinklage[1,2,a], C.D. Beidler[1], P. Helander[1,2], G. Fuchert[1], H. Maassberg[1], K. Rahbarnia[1],

T. Sunn Pedersen[1,2], Y. Turkin[1], R.C. Wolf[1,3], A. Alonso[4], T. Andreeva[1], B. Blackwell[5],

S. Bozhenkov[1], B. Buttenschön[1], A. Czarnecka[6], F. Effenberg[7], Y. Feng[1], J. Geiger[1], M.

Hirsch[1], U. Höfel[1], M. Jakubowski[1], T. Klinger[1,2], J. Knauer[1], G. Kocsis[8], A. Krämer-

Flecken[9], M. Kubkowska[6], A. Langenberg[1], H.P. Laqua[1], N. Marushchenko[1], A. Mollén[1], U.

Neuner[1], H. Niemann[1], E. Pasch[1], N. Pablant[10], L. Rudischhauser[1], H.M. Smith[1], O.

Schmitz[7], T. Stange[1], T. Szepesi[7], G. Weir[1], T. Windisch[1], G.A. Wurden[11], D. Zhang[1]

and the W7-X Team

[1]Max-Planck-Institut für Plasmaphysik, Greifswald, Germany

[2]E.-M.-Arndt Universität Greifswald, Greifswald, Germany

[3]Technische Universität Berlin, Berlin, Germany

[4]CIEMAT, Madrid, Spain

[5]Australian National University, Canberra, Australia

[6]IPPLM, Warsaw, Poland

[7]U Wisconsin, Madison, WI, USA

[8]Wigner RCP RMI, Budapest, Hungary

[9]FZJ, Jülich, Germany

[10]Princeton Plasma Physics Laboratory, Princeton, NJ, 08543, USA

[11]LANL, Los Alamos, NM, USA

[a]Corresponding author. E-mail: dinklage@ipp.mpg.de

ORCID IDs

A. Dinklage https://orcid.org/0000-0002-5815-8463

R.C. Wolf https://orcid.org/0000-0002-2606-5289

T. Andreeva https://orcid.org/0000-0003-2390-4240

S. Bozhenkov, https://orcid.org/0000-0003-4289-3532

F. Effenberg https://orcid.org/0000-0002-4846-4598

U. Höfel https://orcid.org/0000-0003-0971-5937

A. Krämer-Flecken https://orcid.org/0000-0003-4146-5085

N. Pablant https://orcid.org/0000-0001-6617-8459

L. Rudischhauser https://orcid.org/0000-0002-3696-7067

G.A. Wurden https://orcid.org/0000-0003-2991-1484

The two leading concepts for confining high-temperature fusion plasmas are the tokamak and the stellarator. Tokamaks are rotationally symmetric and use a large plasma current to achieve confinement, whereas stellarators are non-axisymmetric and employ three-dimensionally shaped magnetic field coils to twist the field and confine the plasma. As a result, the magnetic field of a stellarator needs to be carefully designed to minimise the collisional transport arising from poorly confined particle orbits, which would otherwise cause excessive power losses at high plasma temperatures. In addition, this type of transport leads to the appearance of a net toroidal plasma current, the so-called bootstrap current. Here, we analyse results from the first experimental campaign of the Wendelstein 7-X stellarator, showing that its magnetic-field design allows good control of bootstrap currents and collisional transport. The energy confinement time is among the best ever achieved in stellarators both in absolute figures ($\tau_E > 100$ms) and relative to the stellarator confinement scaling. The bootstrap current responds as predicted to changes in the magnetic mirror ratio. These initial experiments confirm several theoretically predicted properties of W7-X plasmas, and already indicate consistency with optimisation measures.

Both tokamaks and stellarators use helical magnetic fields that trace out toroidal magnetic flux surfaces to confine fusion-grade plasmas [1,2], but the magnetic-field geometry of the two concepts is fundamentally different. In the tokamak, the magnetic field strength B varies from the inside of the torus to the outside, but is constant in the toroidal direction. (Toroidal refers to the long way around the torus, poloidal to the short way.) This toroidal symmetry results in the conservation of the (canonical) angular momentum of each particle, which implies that collisionless particle trajectories are confined within the plasma. A fusion plasma is of course not collisionless –collisions are required to produce fusion reactions – but the collision frequency is so low that the confinement is very poor unless most collisionless orbits are well confined. Because stellarators lack toroidal symmetry, particles trapped in magnetic mirrors (local minima of the field strength) along the field can drift out of the plasma confinement region. Already half a century ago, it was recognised that the collisional transport is strongly affected by the geometry of the collisionless orbits [3]. While in tokamaks this so-called neoclassical transport is usually unimportant compared with the energy loss caused by plasma turbulence, the neoclassical losses in stellarators can become very large at high plasma temperature T and for the fast α-particles produced in deuterium-tritium fusion reactions.

The transport coefficients in stellarators depend sensitively on the collision frequency ν as well as the drift velocity $v_D \sim mv^2/(2qRB)$ (where v denotes the speed, m the mass and q the charge of the particles in question and R is the major radius of the device) and the radial electric field E_r perpendicular to the magnetic surfaces. When the latter is small and the mean free path between collisions is long, the transport coefficient usually scales as $D^{1/\nu} \propto v_D^2/\nu \propto T^{7/2}$ (Strictly speaking, it is the so-called mono-energetic radial transport coefficient that scales this way. It refers to the transport of particles with a definite energy, whereas the total transport is obtained by an average over the energy distribution of all particles, see also supplementary Fig. 1.), resulting in an energy flux proportional to $T^{9/2}$. The neoclassical transport can be moderated by the electric field, E_r, which acts to confine the drift motion of

the trapped particles and results in a modified scaling of the radial transport as $D^{\sqrt{\nu}} \propto$

$v_D^2 E_r^{-3/2} \sqrt{\nu} \propto T^{5/4} E_r^{-3/2}$ depending, as it were, more favourably on the collision frequency and

temperature.

Each of these scalings also has an associated 'geometrical factor' which describes the

influence of the magnetic-field geometry on the transport. For $1/\nu$ transport it is conventional

in the literature, e.g. [4], to express this factor in terms of the effective helical ripple, ε_{eff},

which combines all information concerning the number of trapped particles and their average

radial drifts into a single figure-of-merit. In classical (non-optimized) stellarators, ε_{eff} is as

large as the actual helical ripple of the device. Since $1/\nu$ transport scales as $\varepsilon_{\text{eff}}^{3/2}$, the energy

losses in such devices become prohibitive for a burning fusion plasma unless the product RB

is chosen sufficiently large. The geometrical factor of $\sqrt{\nu}$ transport generally receives little

attention – its influence on neoclassical confinement is of secondary importance to that of the

radial electric field for this regime – but it will be of relevance for understanding the W7-X

results presented below. The $\sqrt{\nu}$ geometrical factor is often different for differing magnetic

configurations but is the same for the two cases investigated here.

The $1/\nu$ and $\sqrt{\nu}$ regimes are peculiar to stellarators and do not exist in axisymmetric

tokamaks. A further difference is that the neoclassical transport is not ``intrinsically

ambipolar'' in stellarators: The electron and ion particle fluxes are in general unequal and

depend differently on the electric field. E_r therefore adjusts to whatever value is required to

keep the electron and ion charge fluxes equal and opposite. The resulting equation for E_r is

nonlinear and can have several solutions (roots), which themselves depend on the local

plasma parameters. When the density is high, the electron and ion temperatures approach

each other due to collisional energy exchange, and the so-called ion root appears. Here the

radial electric field points towards the plasma centre. At lower densities and with predominant

electron heating, the electron temperature is often significantly higher than the ion

temperature, and the electric field reverses sign; here one speaks of the electron root [5].

At temperatures and densities required to achieve a burning deuterium-tritium plasma (T=10 – 20 keV and n~10^{20} m^{-3}), stellarator plasmas are usually in the ion-root transport regime. The electric field then reduces the ion fluxes (in the $\sqrt{v}$ transport regime) to match the electron flux (in the $1/v$ transport regime) [6]. The resulting $1/v$ transport with its unfavourable temperature dependence was long considered to be a show-stopper for stellarators. A way to mitigate the losses was proposed by Palumbo [7], who proposed to tailor the magnetic field so that the magnetic drifts across the flux surfaces vanishes everywhere. Such, so-called isodynamic, fields cannot be achieved in toroidal geometry, but it was later realised that the average drift could be made very small for most orbits. Such configurations, where trapped particles remain on poloidally closed drift surfaces and do not drift out of the plasma, are called quasi-isodynamic [8] and enjoy much better neoclassical confinement than the classical stellarator.

To really device a stellarator that can confine and sustain a high-temperature fusion plasma long enough (at least of the order of hours), much more than the neoclassical confinement has to be considered. With the advent of powerful computers, it has become possible to find magnetic field configurations which simultaneously fulfil a number of requirements, including low neoclassical transport, sufficient plasma stability at volume averaged β-values (ratio between plasma pressure and magnetic field pressure) up to 5%, and a workable exhaust concept for removing heat and particles from the plasma. The magnetic field has to be generated by shaped (superconducting) field coils that can be constructed and assembled without too much difficulty. The type of configuration resulting from this optimisation procedure for W7-X was termed the helical-axis advanced stellarator, in short HELIAS [9]. The stellarator W7-X is the first large, super-conducting machine of the HELIAS line.

Self-generated plasma currents - the bootstrap current, the Pfirsch-Schlüter current and the diamagnetic current - always arise in magnetised plasmas, and the HELIAS concept seeks to minimise these currents and their effect on the magnetic-field geometry. The bootstrap current is a net toroidal current driven by the pressure gradient [10,11]. It originates from the

fact that there is a correlation between the parallel (to B) velocity and the radial position of trapped particles. In a tokamak, the trapped ions move in the direction of the plasma current on the outboard leg of their (banana) orbit and in the opposite direction on the inboard leg. The opposite is true for the electrons, so if there is a pressure gradient across a given magnetic surface, the number of co-current-moving particles of either species is different from that of the counter-moving ones, and a net current arises. Something similar happens in stellarators, but the relation between parallel velocity and radial position along particle orbits is different, and so is therefore the bootstrap current. Its direction depends on the magnetic geometry, and W7-X has been optimised to make it as small as possible. The bootstrap current has been observed experimentally both in tokamaks [12] and stellarators [13], and agrees broadly with theoretical expectations.

The bootstrap current vanishes exactly in a perfectly quasi-isodynamic field [14, 15]. Due to imperfect optimisation, it remains finite in W7-X but it is nevertheless much smaller than in a typical tokamak. Going from the plasma edge to the centre, the rotational transform ɨ decreases only slightly. This means ɨ can be chosen in such a way that resonances corresponding to low-order rational values of ɨ are avoided. Such resonances usually lead to a degradation of confinement by the formation of magnetic islands. If ɨ is close to unity at the plasma edge, the resulting magnetic islands can be used to divert the edge plasma to specially designed target plates. Since the formation and position of those islands sensitively depend on the precise value of ɨ, even small plasma currents need to be controlled.

The carefully tailored magnetic field of W7-X is created by a set of shaped magnetic field coils. Fig. 1 shows the main components of the device: 50 modular, non-planar coils generate the confining magnetic field, while 20 planar coils can be used to adjust the rotational transform and change the radial position of the plasma. The coils are superconducting to allow for steady-state plasma operation. The magnetic field has five-fold symmetry and forms five linked magnetic mirrors.

7

Elements of the coil design were already tested on the predecessor experiment, Wendelstein 7-AS [16]. The modular, non-planar coils of W7-X are shaped in such a way that the resulting field geometry meets the different optimization requirements. The coils have to be precisely manufactured and assembled to avoid perturbations of the magnetic field. It has been demonstrated that W7-X possesses nested magnetic surfaces with measured relative field errors $\delta B/B$ smaller than 10^{-5} [17].

The first experimental campaign of W7-X lasted from December 2015 until March 2016. In this phase, the exhaust heat was taken up by five un-cooled graphite limiters designed to follow the last closed flux surface [18]. In order to keep the temperature rise on the limiter surfaces well below the sublimation temperature of graphite, the maximum energy delivered to the plasma during a single pulse was set to 4 MJ.

The main objective of the campaign was the integral commissioning of the device, including first plasma generation, plasma-vessel conditioning, and the successive commissioning of about 30 plasma diagnostics [19]. The commissioning phase could be conducted without major problems and about half of the time was used for physics studies, which despite the brevity of the campaign lead to a wealth of results [20,21,22]. Plasma experiments were limited to relatively low plasma density, thus precluding high plasma pressure and access to the $1/\nu$ regime for which the magnetic field was mainly optimised. Over the coming years, a staged approach will be taken to attain steady-state operation in relevant collisionality regimes at high heating power [23].

A key question was whether aspects of the W7-X optimisation could already be verified in spite of the technical limitations for the first campaign (e.g. limited heating power, density, pulse length, plasma pressure). To investigate the effect of the magnetic field geometry on heat transport and plasma currents, two configurations with different magnetic mirror ratios were created by adjusting the ratio of the currents in the planar coils of type A and B (cf. Fig. 1**b**), which alters the depth of the toroidal magnetic mirror. The mirror ratio is given by the maximum and minimum field strengths along the magnetic axis as $(B_{\max} - B_{\min})/(B_{\max} +$

B_{min}). Setting $I_B/I_A = 0$ causes the magnetic induction in the straight sections of the pentagon to be reduced and thus gives a 'higher-mirror' configuration (red lines throughout this paper, mirror ratio 6.0%). The current ratio $I_B/I_A = 1$ results in a 'lower-mirror' configuration (blue lines, mirror ratio 3.7%). In the Fourier representation of the magnetic field (Fig. 2**a**), the decrease of the mirror ratio is reflected by the toroidal mirror term $\tilde{b}_{01}$ (more details in the Methods section).

This change in the coil currents directly affects the number of trapped particles and their orbits, but only slightly increases the rotational transform, leading to an inward shift of the island chain at the $\iota = 5/6$ surface (Fig. 2**b**). The effective helical ripple $\varepsilon_{\mathrm{eff}}$ affects the $1/\nu$ plasma transport, as mentioned above, and is about half as large in the lower-mirror case as in the higher-mirror case (Fig. 2**c**). The configuration effect on the plasma parameters is shown in Fig. 3. For both configurations, the heating power was set to 1.0 MW for one second and lowered to about 0.6 MW for the remaining 5 s. Given the energy limit of 4 MJ, these settings allowed for a total pulse length of 6 s. Power losses by radiation P_{rad} and convective heat losses onto the limiters P_{limiter} add up to more than 80% of the total heating power (Fig. 3(a)) [24]. The remaining 20% presumably leave the plasma by charge-exchange processes with neutrals that are released by the plasma-facing components, and may also stem from measurement errors (discussed in the methods section). The power traces in the higher- and lower-mirror cases are nearly identical, indicating that the power-loss mechanisms are similar. The plasma line density (Fig. 3**b**) is stationary after a few hundred ms and stays constant, indicating full recycling of plasma particles since no additional gas fuelling was applied. Such stationary plasma densities required dedicated glow-discharge-cleaning of the in-vessel components. The confinement quality is represented by the temporal evolution of the plasma diamagnetic energy (Fig.3**c**), which remains constant or decays slightly during phases of constant heating power.

Fig. 4 shows the energy confinement time $\tau_E = W/P$, with W the stored plasma thermal energy and P the heating power, plotted against scaling expectations (ISS04 scaling [25]).

The figure also contains the W7-X discharge with highest $\tau_E/\tau_{ISS04.}$ [(128±25)ms/(117±14)ms, see supplementary Table 1 and 2] and results from LHD (inward-shifted configuration) with best confinement [25].

The energy confinement times of early W7-X discharges are among the highest attained in stellarators. A comparison with similar discharge conditions in W7-AS indicates significant improvement in terms of the confinement factor τ_{exp}/τ_{ISS04} (taking differences in geometry, heating power and density into account) seen as an increase with respect to the magenta line in Fig. 4. Comparing with tokamak data (rephrased to the stellarator scaling ISS04 [26,27]), the energy confinement time of W7-X limiter plasmas [28] is well within the range of tokamak high-confinement (H-mode) plasmas, which is the reference for achieving a burning fusion plasma in ITER ($P_{fusion}/P_{heating} = 10$) [29].

While the global confinement is less affected by changes in the mirror ratio than would be expected from $1/\nu$ transport, the toroidal plasma current responds more sensitively, (cf. Fig. 3**d**). The measurements show after 6 s rising but saturating plasma currents. At the end of the discharge, the plasma current in the lower-mirror case is 2.15 kA and in the higher-mirror case 1.47 kA.

This difference in plasma current but similarity in energy transport can be explained within neoclassical physics. As an input for modelling, Fig. 5 shows the profiles of temperatures and densities for the lower- (Fig. 5**a**,**b**) and higher-mirror configuration (Fig. 5 **c**,**d**). For both cases, the central electron temperature T_e is higher than the ion temperature T_i, but all profiles are quite similar for the two configurations indicating any gradient driven fluxes to be subordinately affected by the configuration change. For the low densities as shown in Fig.5 **b, g**, the resilience of T_e against changes of the effective ripple and the peaked T_e are signatures for core electron root confinement (CERC with $E_r > 0$).

Fig. 6 displays modelling results supporting the indications for CERC. Figs. 6**a,d**, show radial electric fields calculated with a neoclassical transport model (NTSS [30]) using the profile fits

(Fig. 5). The modelled E_r are confronted with measurements and both indicate a transition to $E_r > 0$ in the plasma centre, again giving evidence for CERC. Energy fluxes from the same modelling are compared to heating sources and radiative losses in Figs. 6**b, d.** The calculated neoclassical energy fluxes are about the same for the two configurations. Thus, the neoclassical energy flux (and the anomalous energy flux) in the two magnetic mirrors cases do not vary with $\varepsilon_{eff}{}^{3/2}$ as for neoclassical $1/\nu$ transport (lower mirror $\varepsilon_{eff} \approx 0.7\%$, higher-mirror $\varepsilon_{eff} \approx 1.3\%$,). All these aspects give evidence that the neoclassical energy transport in the plasma center is in the CERC regime with $\sqrt{\nu}$ transport mainly carried by the electrons.

The specific neoclassical physics is revealed with first-principle calculations of the transport coefficients (supplementary Fig. 1). Since the $\sqrt{\nu}$ transport coefficients are about the same for the two configurations at the experimental plasma conditions, the geometric factor for $\sqrt{\nu}$ energy transport coefficients is about the same as well. The reason lies in the W7-X optimisation which led to a very strong 3D shaping of the plasma. The resulting average elongations of the plasma flux surfaces (defined as $\equiv \left(\epsilon_t / \tilde{b}_{10}\right)^2$) are in excess of five. In this formula, $\epsilon_t = r_{\text{eff}}/R$ is the inverse aspect ratio and $\tilde{b}_{10}$ is the average toroidal curvature term in the Fourier spectrum of B (see Fig. 2**a**). This large elongation has a strong influence on the neoclassical transport of W7-X due to strong reduction of the ∇B-drift for single-particle orbits. By convention, the effects of elongation on $1/\nu$ transport are included in the definition of ε_{eff}. Also accounted for in this definition, however, is the number of trapped particles, which is increased significantly by changing from the lower-mirror to the higher-mirror configuration with its larger toroidal mirror term $\tilde{b}_{01}$ (Fig. 2**a**). This is the main reason for the different ε_{eff} values obtained for the two configurations. In contrast, to leading order the geometrical factor of the $\sqrt{\nu}$ regime is simply $1/\kappa$ and, as this term is identical for the two configurations (Fig. 2**a**), one will therefore expect equal levels of $\sqrt{\nu}$ neoclassical transport in both (assuming E_r is also equal).

While the $\sqrt{\nu}$ energy transport is the same, the neoclassical bootstrap coefficients are different for the two configurations. The calculated bootstrap current profile shows a higher current density for the lower-mirror case (Fig.6**c**) than for the higher-mirror case (Fig.6**f**). The integrated profiles give stationary bootstrap currents I_{BS}^{∞}. This result from neoclassical modelling can be confronted with plasma current measurements as shown in Fig. 3**d** . The toroidal current in is still far from being saturated ($\tau_{L/R} \sim 20\ s$ for these discharges, the time scale is given by the ratio of plasma inductance L to the plasma resistance R), but extrapolates well to the steady-state values predicted from theory. The ratio of measured currents at the end of the plasma at t=6 s ($I_{higher\ mirror}/I_{lower\ mirror}$ = (1.47±0.15)kA/(2.15±0.22)kA = 0.69±0.10) shows good agreement with the ratio of the calculated stationary bootstrap current values ($I_{BS\text{-}higher\ mirror}^{\infty}/I_{BS\text{-}lower\ mirror}^{\infty}$ = 0.61±0.15). A numerical calculation of an equivalent tokamak discharge with the same profiles shows a factor of 3.5 larger bootstrap current, clearly inconsistent with our measurements. Thus, our measurements match the expectations for W7-X closely. This confirms an important aspect of the W7-X optimisation, which was to minimise the absolute value of the bootstrap current in order to control the location of the edge magnetic islands [31].

It is concluded that these results from the first experimental campaign of W7-X seem to confirm important aspects of the optimisation that went into the design of the device, namely the minimization and control of the bootstrap current by the magnetic configuration. In future campaigns, significantly higher performance and a much more comprehensive exploration of the parameter space should be possible. This will allow more detailed studies and a systematic verification of the W7-X optimisation at high plasma pressures not attainable in the first operation phase.

Acknowledgements

Data availability

The data that support the plots within this paper and other findings of this study are available from the corresponding author upon reasonable request.

Author Contributions

AD, CDB, PH, TSP, RCW and TK wrote the paper. AD, TSP, SB, FE and JG prepared the configuration changes and the discharge program. AD, HM, YT, TA, AA, CDB, FE, YF, JG, AM, NM, HMS and OS did modeling and data validation. KR, BB, BB, AC, GF, MH, UH, MJ, JK, GK, AKF, MK, AL, HL, UN, HN, EP, NP, LR, TS, TS, GW, TW, GW and DZ did measurements and data analysis.

Competing financial interests

The authors declare no competing financial interests.

References

[1] L. Spitzer, The Stellarator Concept, Phys. Fluids **1**, 253 – 264 (1958)

[2] P. Helander, C.D. Beidler, T.M. Bird, M. Drevlak, Y. Feng, R. Hatzky, F. Jenko, R. Kleiber, J.H.E. Proll, Yu. Turkin and P. Xanthopoulos, Stellarator and tokamak plasmas: a comparison, Plasma Phys. Contr. Fusion **54**, 124009 (12pp) (2012)

[3] A. A. Galeev, R. Z. Sagdeev, H. P. Furth and M. N. Rosenbluth, Plasma Diffusion in a Toroidal Stellarator, Phys. Rev. Lett. **22**, 511 - 514 (1969)

[4] C.D. Beidler and W.N.G Hitchon, Ripple transport in helical-axis advanced stellarators: a comparison with classical stellarators/torsatrons, Plasma Phys. Contr. Fusion **36**, 317 - 353 (1995)

[5] M. Yokoyama, H. Maaßberg, C.D. Beidler, V. Tribaldos, K. Ida, T. Estrada, F. Castejon, A. Fujisawa, T. Minami, T. Shimozuma, Y. Takeiri, A. Dinklage, S. Murakami and H. Yamada, Core electron-root confinement (CERC) in helical plasmas, Nucl. Fusion **47**, 1213 - 1219 (2007)

[6] A.A. Galeev and R.Z. Sagdeev, Theory of neoclassical diffusion, Reviews of Plasma Physics, vol. 7, ed M.A. Leontovich (New York: Consultants Bureau), pp 257 - 343 (1979) (ISBN: 0-306-17067-1)

[7] D. Palumbo, Some considerations on closed configurations of magnetohydrostatic equilibrium, Nuovo Cimento B **X53**, 507 - 511 (1968)

[8] J. Nührenberg, Development of quasi-isodynamic stellarators, Plasma Phys. Contr. Fusion **52**, 124003 (7pp) (2010)

[9] J. Nührenberg and R. Zille, Stable stellarators with medium β and aspect ratio, Phys. Lett A **114**, 129 – 132 (1986)

[10] A.A. Galeev, Diffusion-electrical phenomena in a plasma confined in a tokamak machine, Sov. Phys. JETP **32**, 752 – 757 (1971)

[11] R.J. Bickerton, J. W. Connor and J. B. Taylor, Diffusion driven plasma currents and bootstrap tokamak, Nature (London) Phys. Sci. **229**, 110 – 112 (1971)

[12] M. C. Zarnstorff, M. G. Bell, M. Bitter, R. J. Goldston, B. Grek, R. J. Hawryluk, K. Hill, D. Johnson, D. McCune, H. Park, A. Ramsey, G. Taylor and R. Wieland, Bootstrap current in TFTR, Phys. Rev. Lett. **60**, 1306 – 1309 (1988)

[13] M. Murakami, B. A. Carreras, L. R. Baylor, G. L. Bell, T. S. Bigelow, A. C. England, J. C. Glowienka, H. C. Howe, T. C. Jernigan, D. K. Lee, V. E. Lynch, C. H. Ma, D. A. Rasmussen, J. S. Tolliver, M. R. Wade, J. B. Wilgen and W. R. Wing, Bootstrap-current experiments in a toroidal plasma-confinement device, Phys. Rev. Lett. **66**, 707 – 710 (1991)

[14] P. Helander and J. Nührenberg, Bootstrap current and neoclassical transport in quasi-isodynamic stellarators, Plasma Phys. Contr. Fusion **51**, 055004 (9pp) (2009)

[15] M. Landreman and P.J. Catto, Omnigenity as generalized quasisymmetry, Phys. Plasmas **19**, 056103-1 - 056103-16 (2012)

[16] M. Hirsch, J. Baldzuhn, C. Beidler, R. Brakel, R. Burhenn, A. Dinklage, H. Ehmler, M. Endler, V. Erckmann, Y. Feng, J. Geiger, L. Giannone, G. Grieger, P. Grigull, H.-J. Hartfuß, D. Hartmann, R. Jaenicke, R. König, H. P. Laqua, H. Maaßberg, K. McCormick, F. Sardei, E. Speth, U. Stroth, F. Wagner, A. Weller, A. Werner, H. Wobig, S. Zoletnik and for the W7-AS Team, Major results from the stellarator Wendelstein 7-AS, Plasma Phys. Contr. **50**, 053001 (204pp) (2008)

[17] T. Sunn Pedersen, M. Otte, S. Lazerson, P. Helander, S. Bozhenkov, C. Biedermann, T. Klinger, R. C. Wolf, H. -S. Bosch and The W7-X Team, Confirmation of the topology of the Wendelstein 7-X magnetic field to better than 1:100,000, Nature Comm. **7**, 13493 (8pp) (2016)

15

[18] S.A. Bozhenkov, M.W. Jakubowski, H. Niemann, S.A. Lazerson, G.A. Wurden, C. Biedermann, G. Kocsis, R. König, F. Pisano, L. Stephey, T. Szepesi, U. Wenzel, T. Sunn Pedersen and R.C. Wolf, Effect of error field correction coils on W7-X limiter loads, Nucl. Fusion **57**, 126030 (10pp) (2017)

[19] T. Sunn Pedersen, T. Andreeva, H.-S. Bosch, S. Bozhenkov, F. Effenberg, M. Endler, Y. Feng, D.A. Gates, J. Geiger, D. Hartmann, H. Hölbe, M. Jakubowski, R. König, H.P. Laqua, S. Lazerson, M. Otte, M. Preynas, O. Schmitz, T. Stange, Y. Turkin and the W7-X Team, Plans for the first plasma operation of Wendelstein 7-X , Nucl. Fusion **55,** 126001 (13pp) (2015)

[20] T. Klinger, A. Alonso, S. Bozhenkov, R. Burhenn, A. Dinklage, G. Fuchert, J. Geiger, O. Grulke, A. Langenberg, M. Hirsch, G. Kocsis, J. Knauer, A. Krämer-Flecken, H.P. Laqua, S. Lazerson, M. Landreman, H. Maaßberg, S. Marsen, M. Otte, N. Pablant, E. Pasch, K. Rahbarnia, T. Stange, T. Szepesi, H. Thomsen, P. Traverso, J.L. Velasco, T. Wauters, G. Weir, T. Windisch and the W7-X Team, Performance and properties of the first plasmas of Wendelstein 7-X, Plasma Phys. Contr. Fusion **59**, 014018 (8pp) (2017)

[21] R.C. Wolf, A. Ali, A. Alonso, J. Baldzuhn, C. Beidler, M. Beurskens, C. Biedermann, H.-S. Bosch, S. Bozhenkov, R. Brakel, A. Dinklage, Y. Feng, G. Fuchert, J. Geiger O. Grulke, P. Helander, M. Hirsch, U. Höfel, M. Jakubowski, J. Knauer, G. Kocsis, R. König, P. Kornejew, A. Krämer-Flecken, M. Krychowiak, M. Landreman, A. Langenberg, H.P. Laqua, S. Lazerson, H. Maaßberg, S. Marsen, M. Marushchenko, D. Moseev, H. Niemann, N. Pablant, E. Pasch, K. Rahbarnia, G. Schlisio, T. Stange, T. Sunn Pedersen, J. Svensson, T. Szepesi, H. Trimino Mora, Y. Turkin, T. Wauters, G. Weir, U. Wenzel, T. Windisch, G. Wurden, D. Zhang, I. Abramovic, S. Äkäslompolo, P. Aleynikov, K. Aleynikova, R. Alzbutas, G. Anda, T. Andreeva, E. Ascasibar, J. Assmann, S.-G. Baek, M. Banduch, T. Barbui, M. Barlak, K. Baumann, W. Behr, A. Benndorf, O. Bertuch, W. Biel, D. Birus, B. Blackwell, E. Blanco, M. Blatzheim, T. Bluhm, D. Böckenhoff, P. Bolgert, M. Borchardt, V. Borsuk, J. Boscary, L.-G. Böttger, H. Brand, Ch. Brandt, T. Bräuer, H. Braune, S. Brezinsek, K.-J. Brunner, B. Brünner, R. Burhenn, B. Buttenschön, V. Bykov, I. Calvo, B. Cannas, A. Cappa, A. Carls, L. Carraro, B. Carvalho, F.

16

Castejon, A. Charl, F. Chernyshev, M. Cianciosa, R. Citarella, Ł. Ciupiński, G. Claps, M. Cole, M.J. Cole, F. Cordella, G. Cseh, A. Czarnecka, A. Czermak, K. Czerski, M. Czerwinski, G. Czymek, A. da Molin, A. da Silva, G. Dammertz, J. Danielson, A. de la Pena, S. Degenkolbe, P. Denner, D.P. Dhard, M. Dostal, M. Drevlak, P. Drewelow, Ph. Drews, A. Dudek, G. Dundulis, F. Durodie, P. van Eeten, F. Effenberg, G. Ehrke, M. Endler, D. Ennis, E. Erckmann, H. Esteban, T. Estrada, N. Fahrenkamp, J.-H. Feist, J. Fellinger, H. Fernandes, W.H. Fietz, W. Figacz, J. Fontdecaba, O. Ford, T. Fornal, H. Frerichs, A. Freund, M. Führer, T. Funaba, A. Galkowski, G. Gantenbein, Y. Gao, J. García Regaña, M. Garcia-Munoz, D. Gates, G. Gawlik, B. Geiger, V. Giannella, N. Gierse, A. Gogoleva, B. Goncalves, A. Goriaev, D. Gradic, M. Grahl, J. Green, A. Grosman, H. Grote, M. Gruca, C. Guerard, L. Haiduk, X. Han, F. Harberts, J.H. Harris, H.-J. Hartfuß, D. Hartmann, D. Hathiramani, B. Hein, B. Heinemann, P. Heitzenroeder, S. Henneberg, C. Hennig, J. Hernandez Sanchez, C. Hidalgo, H. Hölbe, K.P. Hollfeld, A. Hölting, D. Höschen, M. Houry, J. Howard, X. Huang, M. Huber, V. Huber, H. Hunger, K. Ida, T. Ilkei, S. Illy, B. Israeli, A. Ivanov, S. Jablonski, J. Jagielski, J. Jelonnek, H. Jenzsch, P. Junghans, J. Kacmarczyk, T. Kaliatka, J.-P. Kallmeyer, U. Kamionka, R. Karalevicius, H. Kasahara, W. Kasparek, N. Kenmochi, M. Keunecke, A. Khilchenko, D. Kinna, R. Kleiber, T. Klinger, M. Knaup, Th. Kobarg, F. Köchl, Y. Kolesnichenko, A. Könies, M. Köppen, J. Koshurinov, R. Koslowski, F. Köster, R. Koziol, M. Krämer, R. Krampitz, P. Kraszewsk, N. Krawczyk, T. Kremeyer, Th. Krings, J. Krom, G. Krzesinski, I. Ksiazek, M. Kubkowska, G. Kühner, T. Kurki-Suonio, S. Kwak, R. Lang, S. Langish, H. Laqua, R. Laube, C. Lechte, M. Lennartz, W. Leonhardt, L. Lewerentz, Y. Liang, Ch. Linsmeier, S. Liu, J.-F. Lobsien, D. Loesser, J. Loizu Cisquella, J. Lore, A. Lorenz, M. Losert, L. Lubyako, A. Lücke, A. Lumsdaine, V. Lutsenko, J. Majano-Brown, O. Marchuk, M. Mardenfeld, P. Marek, S. Massidda, S. Masuzaki, D. Maurer, K. McCarthy, P. McNeely, A. Meier, D. Mellein, B. Mendelevitch, Ph. Mertens, D. Mikkelsen, O. Mishchenko, B. Missal, J. Mittelstaedt, T. Mizuuchi, A. Mollen, V. Moncada, T. Mönnich, T. Morizaki, R. Munk, S. Murakami, F. Musielok, G. Náfrádi, M. Nagel, D. Naujoks, H. Neilson, O. Neubauer, U. Neuner, T. Ngo, R. Nocentini, C. Nührenberg, J. Nührenberg, S. Obermayer, G. Offermanns, K. Ogawa, J. Ongena, J.W.

Oosterbeek, G. Orozco, M. Otte, L. Pacios Rodriguez, W. Pan, N. Panadero, N. Panadero Alvarez, A. Panin, D. Papenfuß, S. Paqay, A. Pavone, E. Pawelec, G. Pelka, X. Peng, V. Perseo, B. Peterson, A. Pieper, D. Pilopp, S. Pingel, F. Pisano, B. Plaum, G. Plunk, M. Povilaitis, J. Preinhaelter, J. Proll, M.-E. Puiatti, A. Puig Sitjes, F. Purps, M. Rack, S. Récsei, A. Reiman, D. Reiter, F. Remppel, S. Renard, R. Riedl, J. Riemann, S. Rimkevicius, K. Riße, A. Rodatos, H. Röhlinger, M. Romé, P. Rong, H.-J. Roscher, B. Roth, L. Rudischhauser, K. Rummel, T. Rummel, A. Runov, N. Rust, L. Ryc, S. Ryosuke, R. Sakamoto, A. Samartsev, M. Sanchez, F. Sano, S. Satake, G. Satheeswaran, J. Schacht, F. Schauer, T. Scherer, A. Schlaich, K.-H. Schlüter, J. Schmitt, H. Schmitz, O. Schmitz, S. Schmuck, M. Schneider, W. Schneider, M. Scholz, P. Scholz, R. Schrittwieser, M. Schröder, T. Schröder, R. Schroeder, H. Schumacher, B. Schweer, B. Shanahan, I.V. Shikhovtsev, M. Sibilia, P. Sinha, S. Sipliä, J. Skodzik, C. Slaby, H. Smith, W. Spiess, D.A. Spong, A. Spring, R. Stadler, B. Standley, L. Stephey, M. Stoneking, U. Stridde, Z. Sulek, C. Surko, Y. Suzuki, V. Szabó, T. Szabolics, Z. Szökefalvi-Nagy, N. Tamura, A. Terra, J. Terry, J. Thomas, H. Thomsen, M. Thumm, C.P. von Thun, D. Timmermann, P. Titus, K. Toi, J.M. Travere, P. Traverso, J. Tretter, H. Tsuchiya, T. Tsujimura, S. Tulipán, M. Turnyanskiy, B. Unterberg, J. Urban, E. Urbonavicius, I. Vakulchyk, S. Valet, B. van Millingen, L. Vela, J.-L. Velasco, M. Vergote, M. Vervier, N. Vianello, H. Viebke, R. Vilbrandt, A. Vorkörper, S. Wadle, F. Wagner, E. Wang, N. Wang, F. Warmer, L. Wegener, J. Weggen, Y. Wei, J. Wendorf, A. Werner, B. Wiegel, F. Wilde, E. Winkler, V. Winters, S. Wolf, J. Wolowski, A. Wright, P. Xanthopoulos, H. Yamada, I. Yamada, R. Yasuhara, M. Yokoyama, J. Zajac, M. Zarnstorff, A. Zeitler, H. Zhang, J. Zhu, M. Zilker, A. Zimbal, A. Zocco, S. Zoletnik and M. Zuin, Major results from the first plasma campaign of the Wendelstein 7-X stellarator, Nucl. Fusion **57,** 102020 (13pp) (2017)

[22] T. Sunn Pedersen, A. Dinklage, Yu. Turkin, R. Wolf, S.A. Bozhenkov, J. Geiger, G. Fuchert, H.-S. Bosch, K. Rahbarnia, H. Thomsen, U. Neuner, T. Klinger, A. Langenberg, H. Trimiño Mora, P. Kornejew, J. Knauer, M. Hirsch, the W7-X Team and N. Pablant, Key results from the first plasma operation phase and outlook for future performance in Wendelstein 7-X, Phys. Plasmas **24**, 055503-1 – 055503-10 (2017)

[23] R.C. Wolf, C. D. Beidler, A. Dinklage, P. Helander, H. P. Laqua, F. Schauer, T. Sunn Pedersen, F. Warmer and W7-X Team, Wendelstein 7-X Program—Demonstration of a Stellarator Option for Fusion Energy, IEEE Trans. Act. Plasma Sci. **44**, 1466 - 1471 (2016)

[24] G.A. Wurden, C. Biedermann, F. Effenberg, M. Jakubowski, H. Niemann, L. Stephey, S. Bozhenkov, S. Brezinsek, J. Fellinger, B. Cannas, F. Pisano, S. Marsen, H.P. Laqua, R. König, O. Schmitz, J.H. Harris, E.A. Unterberg and the W7-X Team, Limiter observations during W7-X first plasmas, Nucl. Fusion **57,** 056036 (11pp) (2017)

[25] H. Yamada, J.H. Harris, A. Dinklage, E. Ascasibar, F. Sano, S. Okamura, J. Talmadge, U. Stroth, A. Kus, S. Murakami, M. Yokoyama, C.D. Beidler, V. Tribaldos, K.Y. Watanabe and Y. Suzuki, Characterization of energy confinement in net-current free plasmas using the extended International Stellarator Database, Nucl. Fusion **45**, 1684 – 1693 (2005)

[26] U. Stroth, M. Murakami, R.A. Dory, H. Yamada, S. Okamura, F. Sano and T. Obiki , Energy confinement scaling from the international stellarator database, Nucl. Fusion **36**, 1063 – 1077 (1996)

[27] A. Dinklage, H. Maaßberg, R. Preuss, Yu.A. Turkin, H. Yamada, E. Ascasibar, C.D. Beidler, H. Funaba, J.H. Harris, A. Kus, S. Murakami, S. Okamura, F. Sano, U. Stroth, Y. Suzuki, J. Talmadge, V. Tribaldos, K.Y. Watanabe, A. Werner, A. Weller and M. Yokoyama, Physics model assessment of the energy confinement time scaling in stellarators, Nucl. Fusion **47**, 1265 – 1273 (2007)

[28] M. Hirsch, A. Dinklage, A. Alonso, G. Fuchert, S. Bozhenkov, U. Höfel, T. Andreeva, J. Baldzuhn, M. Beurskens, H.-S. Bosch, C.D. Beidler, C. Biedermann, E. Blanco, R. Brakel, R. Burhenn, B. Buttenschön, A. Cappa, A. Czarnecka, M. Endler, T. Estrada, T. Fornal, J. Geiger, O. Grulke, J.H. Harris, D. Hartmann, M. Jakubowski, T. Klinger, J. Knauer, G. Kocsis, R. König, P. Kornejew, A. Krämer-Flecken, N. Krawczyk, M. Krychowiak, M. Kubkowska, I. Ksiazek, A. Langenberg, H.P. Laqua, S. Lazerson, H. Maaßberg, N. Marushchenko, S. Marsen, V. Moncada, D. Moseev, D. Naujoks, M. Otte, N. Pablant,

E. Pasch, F. Pisano, K. Rahbarnia, T. Schröder, T. Stange, L. Stephey, T. Szepesi, T. Sunn Pedersen, H. Trimino Mora, H. Thomsen, H. Tsuchiya, Yu. Turkin, T. Wauters, G. Weir, U. Wenzel, A. Werner, R. Wolf, G.A. Wurden, D. Zhang and the W7-X Team, Confinement in Wendelstein 7-X limiter Plasmas, Nucl. Fusion **57**, 086010 (8pp) (2017)

[29] E.J. Doyle, W.A. Houlberg, Y. Kamada, V. Mukhovatov, T.H. Osborne, A. Polevoi, G. Bateman, J.W. Connor, J.G. Cordey, T. Fujita, X. Garbet, T.S. Hahm, L.D. Horton, A.E. Hubbard, F. Imbeaux, F.Jenko, J.E. Kinsey, Y. Kishimoto, J. Li, T.C. Luce, Y. Martin, M. Ossipenko, V. Parail, A. Peeters, T.L. Rhodes, J.E. Rice, C.M. Roach, V. Rozhansky, F. Ryter, G. Saibene, R. Sartori, A.C.C. Sips, J.A. Snipes, M. Sugihara, E.J. Synakowski, H. Takenaga, T. Takizuka, K. Thomsen, M.R. Wade, H.R. Wilson, Chapter 2: Plasma confinement and transport, Nucl Fusion **47**, S18-S127 (2007)

[30] Yu. Turkin, C. D. Beidler, H. Maaßberg, S. Murakami, V. Tribaldos, and A. Wakasa, Neoclassical transport simulations for stellarators, Phys. Plasmas **18**, 022505-1 – 022505-11 (2011)

[31] Yu. Turkin, H. Maaßberg, C.D. Beidler, J. Geiger, and N. Marushchenko, Current control by ECCD for W7-X, Fusion Sci. Technol. **50**, 387 - 394 (2006)

Methods

Plasma generation: For a description of the technical operation of the device W7-X see Ref. [32]. Plasma heating was conducted with electron cyclotron resonance heating (ECRH) equipped with specific protective diagnostics [33]. The heating power was measured with microwave diodes calibrated with calorimetry and stray-radiation was measured to be small for the applied X2 heating [34] resulting in uncertainties for the heating power of +5%/-10%. The working gas (hydrogen) was injected prior to the discharge. The plasma facing components were conditioned by glow discharge cleaning before both experiments.

Magnetic configuration changes: The change in the magnetic configuration was made by changing the operation current in planar coil type B while readjusting the coil current ratios for all other coils to keep the ECRH resonance condition, i.e. to adjust B to 2.5 T in the corner section of the W7-X pentagon. The specific effect on parameters that quantitatively affect the bootstrap current lies in the leading harmonics $\tilde{b}_{mn}$ of the Fourier representation of the magnetic field $(B/B_0 = \sum \tilde{b}_{mn}(cos(m\theta - nN\varphi))$ with m, n the poloidal and toroidal mode numbers, $N = 5$ the number of field periods and θ, φ the poloidal and toroidal angles, respectively. The Fourier harmonics directly enter into the neoclassical transport coefficients [35,36]. Fig. 2**a** illustrates the main effect in the Fourier components of the field to be an increase of the toroidal mirror term $\tilde{b}_{01}$ (with direct influence on the magnetic mirror ratio) when the current in the planar coils of type B is lowered. One notes, however, the toroidal curvature terms $\tilde{b}_{10}$ (and thus the average elongation κ) are identical and the resulting geometrical factors for $\sqrt{\nu}$ transport are likewise identical for the specific case investigated here. Moreover, the helical component of the magnetic field $\tilde{b}_{11}$ is also unaffected by the change of I_B/I_A. The corresponding monenergetic transport coeffcients are shown in the supplementary Figure 1.

Numerics: The properties of the magnetic field geometry were calculated with the MHD equilibrium code VMEC [37]. The VMEC results are used to map the diagnostic data (see below) on flux surfaces labelled with an effective radius r_{eff}. Vacuum field calculations have

been conducted with a field-line tracer code [38]. The neoclassical transport analyses and modelling (E_r, $q_{NC}V'$ and j_{BS} calculations) were conducted with the NTSS [30] code which employed neoclassical transport coefficients from the DKES code [39,40]. The NTSS code and dedicated DKES calculations were also used to conduct calculations for an equivalent tokamak. The SFINCS code [41] with an extended neoclassical model (not relying on the assumption of incompressible $\vec{E} \times \vec{B}$ drifts and using a full inter-species linearized Fokker-Planck operator) was employed for model comparison resulting in about 10% higher bootstrap current than NTSS for the cases discussed in this paper. For both power deposition calculations and electron cyclotron current drive calculations, the ray tracing code TRAVIS [42] was used.

Data validation: For the overall power balance, the heat load patterns on the limiter were validated with plasma edge simulations with the EMC3-EIRENE [43] code. Measurements of the heat flux patterns on the limiters for the two configurations investigated, which formed the boundary between confinement region with closed magnetic field lines and the scrape-off layer with open field lines, showed that changes in these patterns can be explained by variations in the connection lengths of the magnetic field lines in the scrape-off layer [44].

Plasma diagnostics: An overview on W7-X diagnostics is given in Ref. [45]. The radiated power profile was derived by Abel-inversion of measurements from a bolometer array. The inversion does not take asymmetries into account. Overall uncertainties for the radiated power are around 10%. The line density was measured with a dispersion interferometer at relative errors of less than 10%. Line densities from Thomson data were derived from density profiles mapped with VMEC equilibrium calculations on the line of sight of the interferometer. Uncertainties in Fig. 3**b** mainly result from the scatter of Thomson data and measurement errors in the observation channels propagating to relative uncertainties of 10% in the line integral derived from Thomson scattering data. The error in the plasma current measurements with the Rogowski coils [46] is about 10%. The density profiles were measured by Thomson scattering. Spatially resolved electron temperature measurements were conducted with

electron cyclotron radiometry and Thomson scattering. Electron temperatures at the last closed flux surface position were determined from Langmuir-probe measurements. Measurements of line averaged Z_{eff} values were derived from the Bremsstrahlung contribution in pulse height analysis spectra resulting in Z_{eff} = 2.5±1. Ion temperature profiles were derived from a tomographic inversion of X-ray imaging spectroscopy as well as poloidal plasma velocity measurements. The associated errors reflect both the inversion and the radially dependent signal-to-noise ratio of the X-ray emissivity [47]. The diamagnetic energy measurements had systematic offsets of 8% (included in (cf. Fig. 3**c**)) and scatter in comparison with the kinetic energy around 10%. The kinetic energy had a total error of 20% as reflected by the error bars in Fig. 3. Poloidal velocities were also derived from correlation reflectometry with errors considering the correlation procedure [48]. The plasma volume was cross-checked with video camera images. The power deposition profile was checked with heat-wave correlation measurements (ECE) in separate experiments at the same magnetic configuration.

Heat Flux Modeling: The modeling results in Fig. 6**b** and **e** show neoclassical energy fluxes qV' (q being the energy flux density, V' the surface area) calculated from the plasma profiles with NTSS. qV' is compared to the heating power P_{ECRH} with substracted radiated power P_{rad} (from Abel inversion). Charge exchange losses are not accounted for in this analysis. The spatial variation of P_{ECRH} reflects power deposition calculations from the TRAVIS code. Errors are due to the measured ECRH power and bolometer measurements. The TRAVIS calculations deliver also the electron cyclotron current confirming earlier estimates of almost negligible current drive [49] (for the lower mirror case $I_{ECCD}° = (54 \pm 25)$ A and for the higher mirror case $I_{ECCD}° = (60 \pm 25)$ A with errors due to profile and Z_{eff} uncertainties). $q_{NC}V'$ from the NTSS code corresponds up to (63 ± 12)% (lower mirror) and (55 ± 15)% (higher mirror) of the deposited power in the core region (i.e. E_r >0 for $r_{eff}/a < ½$, a is the plasma minor radius). The remaining energy flux is modeled with a phenomenological model $\chi^e_{ano} \sim 1/n$. In order to match the total heat flux $q_{tot}V' = q_{NC}V' + q_{ano}V'$ with $P_{ECRH}-P_{rad}$ in the plasma core ($r_{eff}/a \sim 1/3$), an anomalous heat diffusivity of $\chi_{ano}^e = (0.24\pm0.06)$ m^{2}s^{-1} is required to model the energy flux

(Fig.5**d**, **i**). For $r_{eff}/a > 1/2$, however, the phenomenogical model for anomalous fails and the modeled energy fluxes are significantly lower than P_{ECRH}-$P_{rad.}$ This remains true if the anomalous ion energy fluxes are included and chosen such that the ion energy flux does not exceed the electron-ion collisional transfer power. This choice overestimates the ion heat diffusivity since additional ion energy losses by charge exchange losses are not considered. With these assumptions, the energy fluxes can be modeled as neoclassical energy transport (with dominant $\sqrt{\nu}$ contribution due to almost the same transport coefficients for both configurations (cf. supplementary Figs. 1 and 2)) and anomalous electron energy transport in the core region.   Outside the core region, neoclassical energy fluxes are insufficient to describe the energy fluxes.

References

[32] H.-S. Bosch, R. Brakel, T. Bräuer, V. Bykov, P. van Eeten, J.-H. Feist, F. Füllenbach, M. Gasparotto, H. Grote, T. Klinger, H. Laqua, M. Nagel, D. Naujoks, M. Otte, K. Risse, T. Rummel, J. Schacht, A. Spring, T. Sunn Pedersen, R. Vilbrandt, L. Wegener, A. Werner, R.C. Wolf, J. Baldzuhn, C. Biedermann, H. Braune, R. Burhenn, M. Hirsch, U. Höfel, J. Knauer, P. Kornejew, S. Marsen, T. Stange, H. Trimino Mora and W7-X Team, Final integration, commissioning and start of the Wendelstein 7-X stellarator operation , Nucl. Fusion 57, 116015 (9pp) (2017)

[33] S. Marsen, Y. Corre, H.P. Laqua, V. Moncada, D. Moseev, H. Niemann, M. Preynas, T. Stange and The W7-X Team, First results from protective ECRH diagnostics for Wendelstein 7-X, Nucl. Fusion **57**, 086014 (7pp) (2017)

[34] D. Moseev, H.P. Laqua, S. Marsen, N. Marushchenko, T. Stange, H. Braune, F. Gellert, M. Hirsch, U. Hoefel, J. Knauer, J.W. Oosterbeek, Y. Turkin and the W7-X Team, Inference of the microwave absorption coefficient from stray radiation measurements in Wendelstein 7-X, Nucl. Fusion **57**, 036013 (7pp) (2017)

[35] C.D. Beidler, K. Allmaier, M.Yu. Isaev, S.V. Kasilov, W. Kernbichler, G.O. Leitold, H. Maaßberg, D.R. Mikkelsen, S. Murakami, M. Schmidt, D.A. Spong, V. Tribaldos and A. Wakasa, Benchmarking of the mono-energetic transport coefficients—results from the International Collaboration on Neoclassical Transport in Stellarators (ICNTS), Nucl. Fusion **51**, 076001 (28pp) (2011)

[36] C. Beidler, G. Grieger, F. Herrnegger, E. Harmeyer, J. Kisslinger, W. Lotz, H. Maassberg, P. Merkel, J. Nührenberg, F. Rau, J. Sapper, F. Sardei, R. Scardovelli, A. Schlüter and H. Wobig, Physics and Engineering Design for Wendelstein VII-X, Fusion Technol. **17**, 148 - 168 (1990)

[37] S.P. Hirshman, W.I. van Rij and P. Merkel, Three-dimensional free boundary calculations using a spectral Green's function method, Comp. Phys. Comm. **43**, 143 - 155 (1986)

[38] S.A. Bozhenkov, J. Geiger, M. Grahl, J. Kißlinger, A. Werner, R.C. Wolf, Service oriented architecture for scientific analysis at W7-X. An example of a field line tracer, Fusion Eng. Des**. 88**, 2997 – 3006 (2013)

[39] S.P. Hirshman, K. C. Shaing, W. I. van Rij, and E. C. Crume Jr., Plasma transport coefficients for nonsymmetric toroidal confinement systems, Physics of Fluids **29**, 2951 - 2959 (1986)

[40] W.I. van Rij and S.P. Hirshman, Variational bounds for transport coefficients in three-dimensional toroidal plasmas , Phys. Fluids B **1**, 563 – 569 (1989)

[41] M. Landreman, H. M. Smith, A. Mollén, and P. Helander, Comparison of particle trajectories and collision operators for collisional transport in nonaxisymmetric plasmas, Phys. Plasmas **21**, 042503-1 – 042503-16 (2014)

[42] N. Marushchenko, Yu. Turkin, and H. Maaßberg, Ray-tracing code TRAVIS for ECR heating, EC current drive and ECE diagnostic, Comp. Phys. Comm. **185**, 165 – 176 (2014)

[43] Y. Feng, F. Sardei, J. Kisslinger, P. Grigull, K. Mc Cormick, and D. Reiter, 3D Edge Modeling and Island Divertor Physics, Contrib. Plasma Phys. **44**, 57 - 69 (2004)

[44] F. Effenberg, Y. Feng, O. Schmitz, H. Frerichs, S.A. Bozhenkov, H. Hölbe, R. König, M. Krychowiak, T. Sunn Pedersen, D. Reiter, L. Stephey and the W7-X Team, Numerical investigation of plasma edge transport and limiter heat fluxes in Wendelstein 7-X startup plasmas with EMC3-EIRENE , Nucl. Fusion **57,** 036021 (15pp) (2017)

 [45] M. Krychowiak, A. Adnan, A. Alonso, T. Andreeva, J. Baldzuhn, T. Barbui, M. Beurskens, W. Biel, C. Biedermann, B. D. Blackwell, H. S. Bosch, S. Bozhenkov, R. Brakel, T. Bräuer, B. Brotas de Carvalho, R. Burhenn, B. Buttenschön, A. Cappa, G. Cseh, A. Czarnecka, A. Dinklage, P. Drews, A. Dzikowicka, F. Effenberg, M. Endler, V. Erckmann, T.

Estrada, O. Ford, T. Fornal, H. Frerichs, G. Fuchert, J. Geiger, O. Grulke, J. H. Harris, H. J. Hartfuß, D. Hartmann, D. Hathiramani, M. Hirsch, U. Höfel, S. Jabłoński, M. W. Jakubowski, J. Kaczmarczyk, T. Klinger, S. Klose, J. Knauer, G. Kocsis, R. König, P. Kornejew, A. Krämer-Flecken, N. Krawczyk, T. Kremeyer, I. Ksiażek, M. Kubkowska, A. Langenberg, H. P. Laqua, M. Laux, S. Lazerson, Y. Liang, S. C. Liu, A. Lorenz, A. O. Marchuk, S. Marsen, V. Moncada, D. Naujoks, H. Neilson, O. Neubauer, U. Neuner, H. Niemann, J.W. Oosterbeek, M. Otte, N. Pablant, E. Pasch, T. Sunn Pedersen, F. Pisano, K. Rahbarnia, L. Ryć, O. Schmitz, S. Schmuck, W. Schneider, T. Schröder, H. Schuhmacher, B. Schweer, B. Standley, T. Stange, L. Stephey, J. Svensson,T. Szabolics, T. Szepesi, H. Thomsen, J.-M. Travere, H. Trimino Mora, H. Tsuchiya, G. M. Weir, U. Wenzel, A. Werner, B. Wiegel, T. Windisch, R. Wolf, G. A. Wurden, D. Zhang, A. Zimbal, S. Zoletnik, and W7-X Team , Overview of diagnostic performance and results for the first operation phase in Wendelstein 7-X, Rev. Sci. Instrum. **87**, 11D304-1 – 11D304-7 (2016)

[46] M . Endler, B. Brucker, V. Bykov, A. Cardella, A. Carls, F. Dobmeier, A. Dudek, J. Fellinger, J. Geiger, K. Grosser, O. Grulke, D. Hartmann, D. Hathiramani, K. Höchel, M. Köppen, R. Laube, U. Neuner, X. Peng, K. Rahbarnia, K. Rummel, T. Sieber, S. Thiel, A. Vorköper, A. Werner, T. Windisch, M.Y. Ye, Engineering design for the magnetic diagnostics of Wendelstein 7-X, Fusion Eng. Design **100**, 468 – 494 (2015)

[47] N.A. Pablant, A. Langenberg, A. Alonso, C.D. Beidler, M. Bitter, S. Bozhenkov, R. Burhenn, M. Beurskens, L. Delgado-Aparicio, A. Dinklage, G. Fuchert, D. Gates, J. Geiger, K.W. Hill, U. Höfel, M. Hirsch, J. Knauer, A. Krämer-Flecken, M. Landreman, S. Lazerson, H. Maassberg, O. Marchuk, S. Massidda, G.H. Neilson, E. Pasch, S. Satake, J. Svennson, P. Traverso, Y. Turkin, P. Valson, J.L. Velasco, G. Weir, T. Windisch, R.C. Wolf, M. Yokoyama, D. Zhang, and the W7-X Team, Core Radial Electric Field and Transport in Wendelstein 7-X Plasmas, Phys. Plasmas **25**, 022508-1 - 022508-7 (2018)

[48] A. Krämer-Flecken, T. Windisch, W. Behr, G. Czymek, P. Drews, G. Fuchert, J. Geiger, O. Grulke, M. Hirsch, M. Knaup, Y. Liang, O. Neubauer, E. Pasch, J. Velasco, W7X-Team,

Investigation of turbulence rotation in limiter plasmas at W7-X with a new installed poloidal correlation reflectometry, Nucl. Fusion **57**, 066023 (8pp) (2017)

[49] M. Romé, V. Erckmann, U. Gasparino, N. Karulin, Electron cyclotron resonance heating and current drive in the W7-X stellarator, Plasma Phys. Contr. Fusion **40**, 511 – 530 (1998)

Fig.1| Outline of Wendelstein 7-X and its magnet system. a shows a schematic CAD drawing of Wendelstein 7-X (© IPP). Going from the inside to the outside the main components are: Plasma, vacuum vessel, superconducting field coils, (niobium-titanium. planar coils: copper-colored, non-planar coils: silver) coil support structure, cryostat vessel with 254 ports providing access to the plasma vessel. The torus has a mean diameter of 11 m and a mean minor radius of about 0.55 m leading to plasma volumes of about 30 m^3. **b** shows the arrangement of the non-planar, modular coils (labeled with numerals) and planar coils (coil type A is close to the pentagon corners, coil type B acts on the straight section of the module).

Fig. 2| Radial profiles of important magnetic field properties. a shows the effective radius (r_{eff}) profiles of the leading Fourier components $\widetilde{b}_{mn}$ of the magnetic field decomposition (see Methods section) relevant to neoclassical transport in W7-X. $\widetilde{b}_{01}$ is the so-called toroidal mirror term, $\widetilde{b}_{10}$ is the average toroidal curvature (relevant term for plasma elongation) and $\widetilde{b}_{11}$ is the helical component. **b** shows the profile of the rotational transform $\iota = \iota/2\pi$ and **c** the profile of the effective helical ripple ε_{eff} for both configurations (red: higher-mirror configuration, blue: lower-mirror configuration).

Fig. 3| Waveforms of plasma discharges. a shows total electron cyclotron heating power P_{ECRH}. The errors include uncertainties from calorimetric calibration and the standard deviation of a microwave diode signal at stationary heating power. The power going to the limiter $P_{limiter}$ is derived from thermography in one of the five stellarator modules. The $P_{limiter}$ error bars represent the range of variation in the infrared heat load total power measurement, due to the corrections for toroidal asymmetry, based on thermocouples in the supporting structure in each of the five modules. The error of the radiated power P_{rad} is the standard deviation of the fluctuation level. **b** shows line densities from interferometry with the error due

to phase measurement calibration. The error of the line density from Thomson scattering data is calculated from upper and lower bounds of fits to the density profiles and errors in the mapping to magnetic coordinates. **c** shows the time evolution of diamagnetic energy for the two discharges. The error band accounts for temperature drifts in the electronics. **d** shows a comparison of the measured plasma current (errors account for electronics drifts) with the total stationary neoclassical bootstrap current I_{BS}^{∞}. The shaded area is derived from integration the lower and upper boundaries of the current density profiles shown in Fig. 5.

Fig. 4| Energy confinement times of Wendelstein 7-X. Energy confinement times τ_E vs scaling expectations τ_{ISS04}. W7-X data refer to cases discussed in this paper and the discharge with the highest confinement enhancement in the first experiment phase (cf. Supplementary Table 1). The errors of Wendelstein 7-X in τ_E are derived from uncertainties in the plasma profiles including errors in the mapping to magnetic coordinates. The errors in scaling expectations τ_{ISS04} result from propagating the errors in the density and power measurements using the nominal values of other scaling parameters (cf. Supplementary Table 2). Tokamak data are rephrased in terms of the stellarator confinement scaling. Confinement data from CERC discharges on W7-AS is included. The magenta line indicates the scaling expectation from these W7-AS data extrapolated to W7-X parameters.

Fig. 5| Temperature and density profiles for different magnetic configurations. a and **b** refer to the lower-mirror configuration, **c** and **d** to the higher-mirror configuration all at the same heating power (t=0.7 s in Fig. 3). The electron temperature (T_e) (**a**, **b**) is measured by Thomson scattering (TS) and electron cyclotron emission (ECE) and with a Langmuir probe at the limiter position (solid gray bar, also position of the last closed flux surface). The errors in the Thomson (TS) data (also density) are standard deviations of T_e and n_e in stationary phases of the discharges. The error of electron cyclotron emission data (ECE) and probe data are standard deviations of the fluctuation level. The ion temperature is measured with X-ray imaging spectroscopy (XICS) and the error bars in the ion temperature and radial

electric field E_r (Fig.6) are found using a monte-carlo method wherein the line-integrated input profiles to the tomographic inversion procedure are varied within their statistical errorbars (based on photon statistics). The profile function was fitted to all data for each quantity; the error bands are a variation of the amplitude parameter to represent the scatter of the data. **b** and **d** display densities of electrons (n_e) and ions (n_i). The electron density fit was determined as for **a** and **c**. n_i was calculated with carbon as impurity species and a variation in the effective charge Z_{eff}. The estimated variation of Z_{eff} includes the errors of the TS profiles and the statistical error of pulse-height spectra. The dotted gray line indicates the core region as separated by the transition from negative (periphery) to positive radial electric field as shown in Fig.6.

Fig. 6| Neoclassical Modelling: radial electric field, energy fluxes and bootstrap current profiles. a – **c** refer to lower-mirror configuration (cf. Figs. 5**a**, **b**), **d**– **f** to the higher-mirror configuration (cf. Figs. 5**c**, **d**). The neoclassical radial electric field is calculated from the profile fits shown in Fig. 5 with the NTSS code (see method section). All error bands in this figure show simulations with the upper and lower bands of the fits (shaded area) and the errors of Z_{eff} (broken lines). **a** and **d** also show radial electric field measurements from XICS (errors from the same procedure as described for Fig. 5). The error of the reflectometry data (**d**) are the standard deviation of poloidal velocities from correlating different reflectometer channels. **b** and **e** show an the effective power deposition profile P_{ECRH}-P_{rad} compared with energy flux densities q through the respective surface area V'. NC indicate neoclassical fluxes derived with NTSS. The modelled total energy fluxes are $q_{tot}V'$. The errors of P_{ECRH}-P_{rad} are due to calibration uncertainties of the microwave diodes calibrated with calorimetry of the heating power measurement and the standard deviation of the bolometer data. Finally, **c** and **f** show the bootstrap current density from NTSS modeling and results from a more comprehensive calculation (SFINCS). The integrated current density profile is used for the comparison to the total plasma current (Fig. 3 **d**).
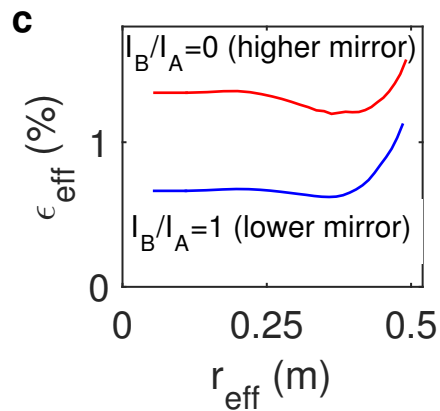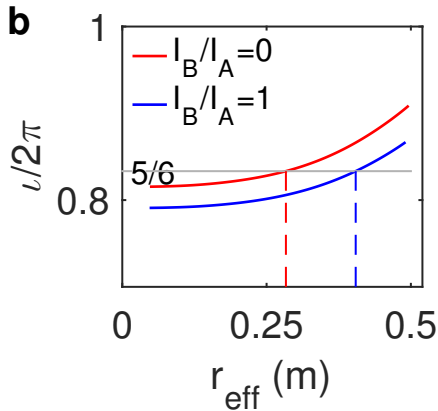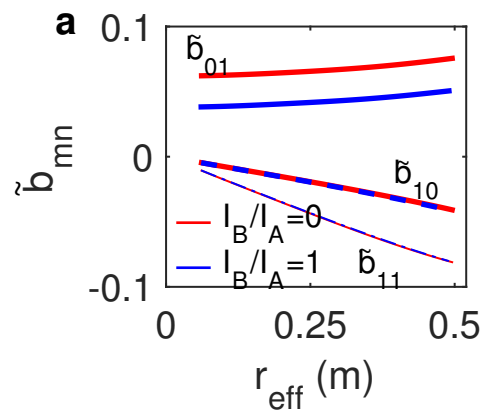
(a)

(b)

1 2 3 4 5 B A

A B 5 4 3 2 1
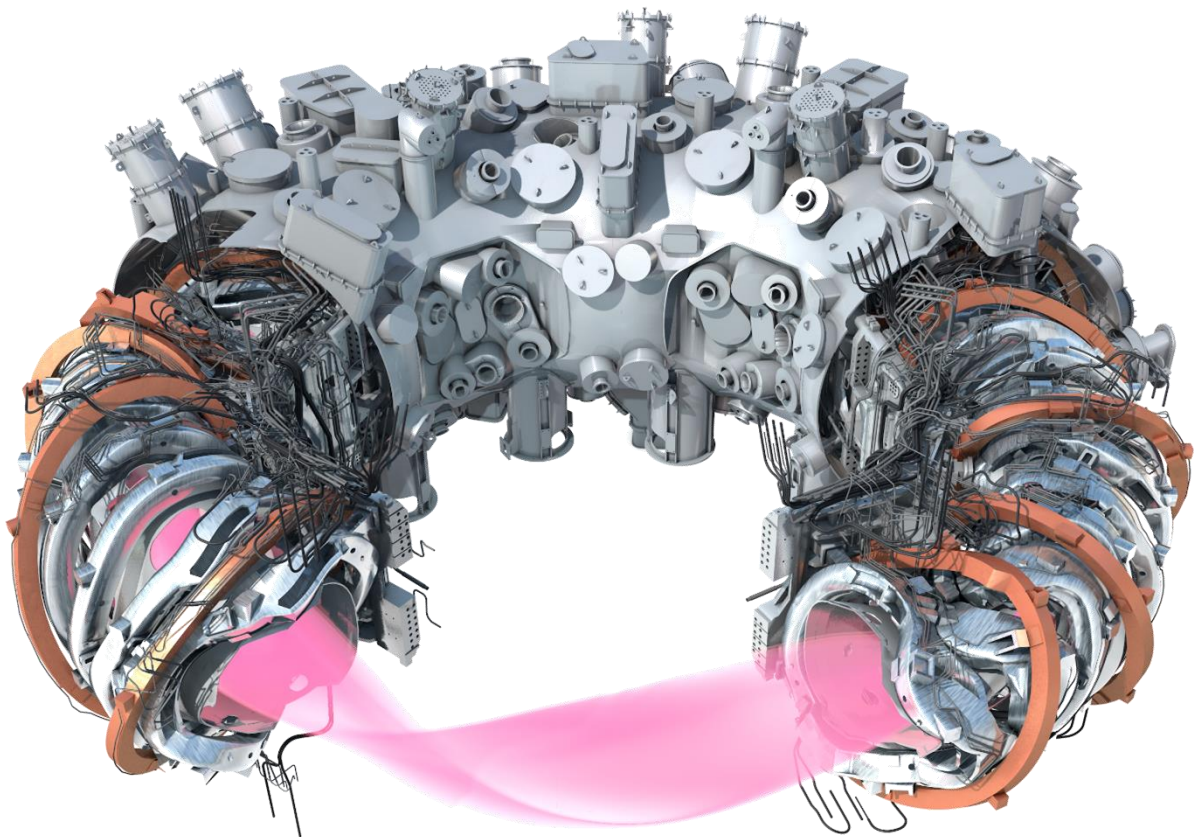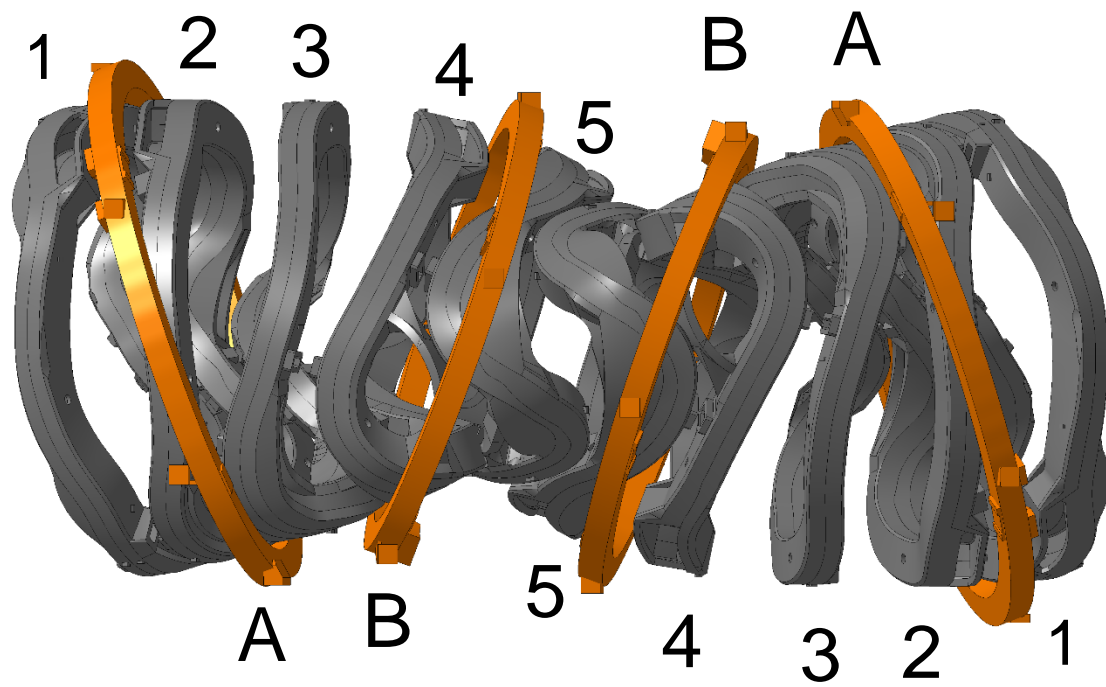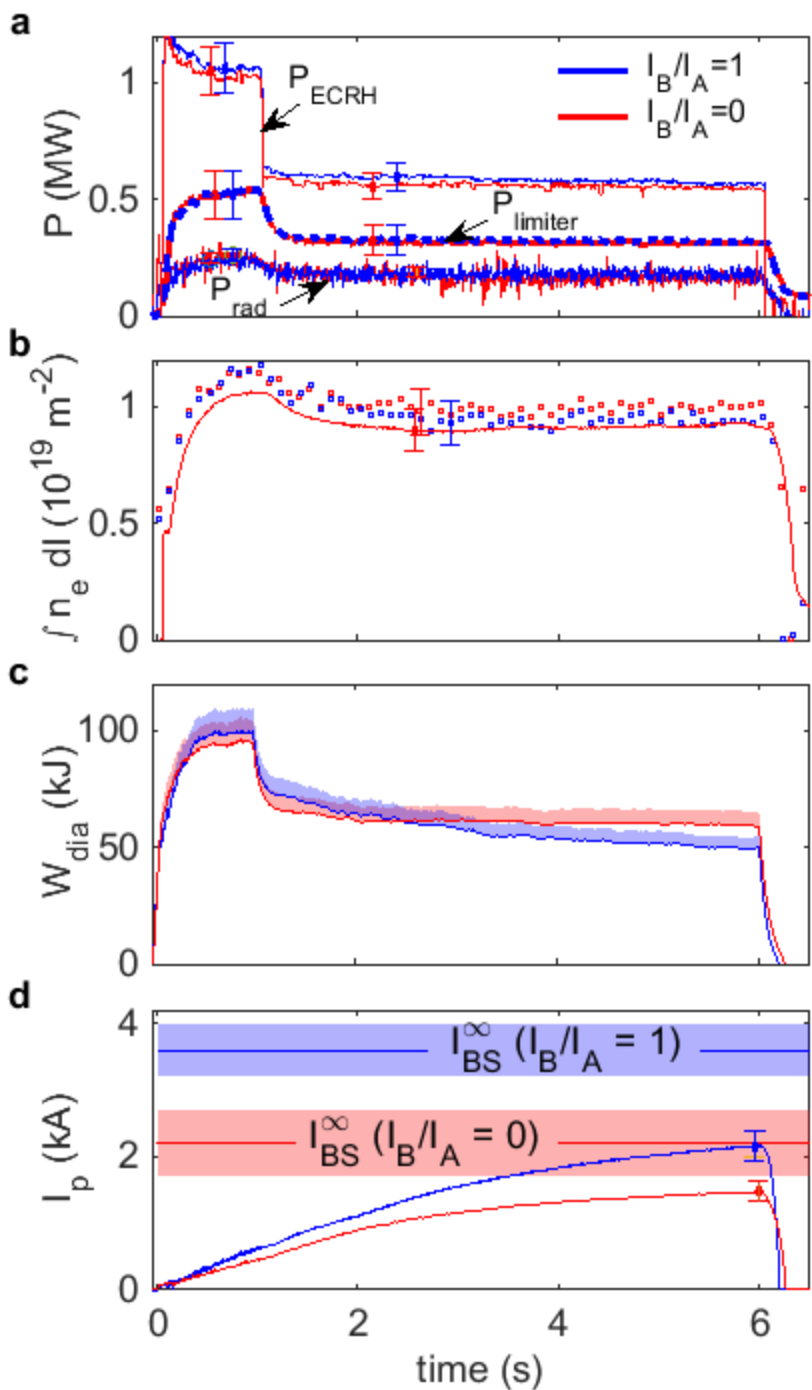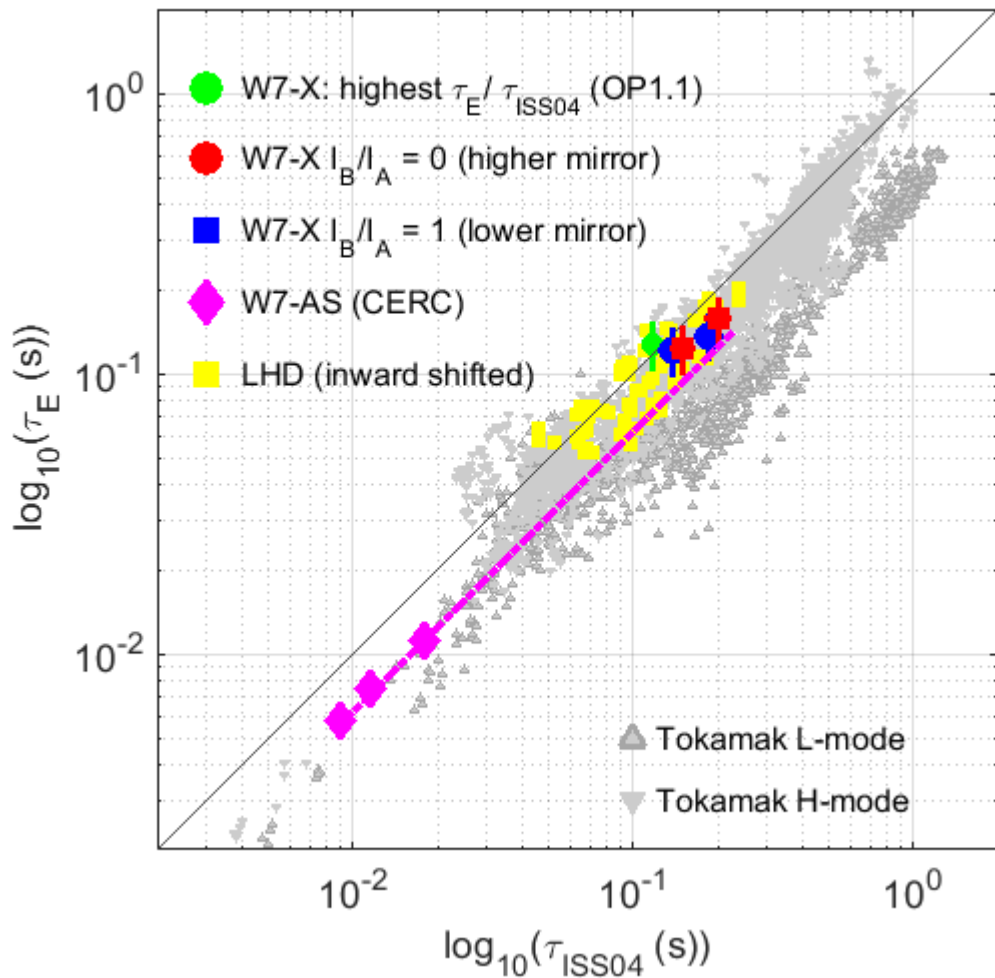
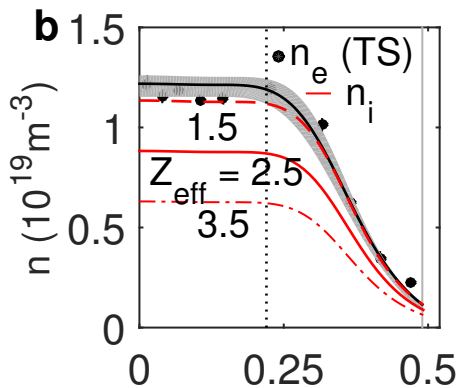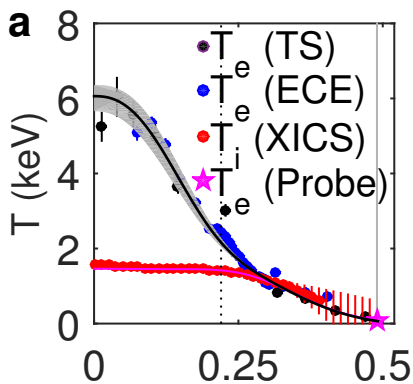higher-mirror configuration: $I_B/I_A = 0$, $\epsilon_{eff} \approx 1.3\,\%$, mirror-ratio $\approx 6.0\,\%$

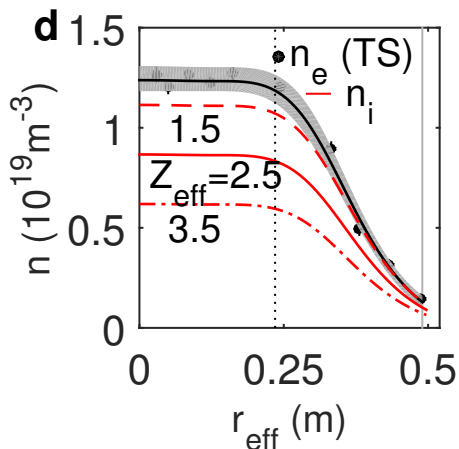lower-mirror configuration: $I_B/I_A = 1$, $\epsilon_{eff} \approx 0.7\,\%$, mirror-ratio $\approx 3.7\,\%$

a

P (MW)

P_{ECRH}

$I_B/I_A = 1$
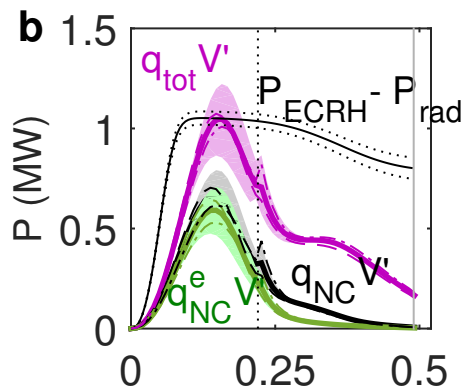$I_B/I_A = 0$

$P_{limiter}$

P_{rad}

b

$\int n_e\, dl$ (10^{19} m^{-2})

c

W_{dia} (kJ)

d

I_p (kA)

I_{BS}^{∞} ($I_B/I_A = 1$)

I_{BS}^{∞} ($I_B/I_A = 0$)

time (s)

Legend:
- W7-X: highest τ_E / τ_{ISS04} (OP1.1)
- W7-X $I_B/I_A = 0$ (higher mirror)
- W7-X $I_B/I_A = 1$ (lower mirror)
- W7-AS (CERC)
- LHD (inward shifted)
- Tokamak L-mode
- Tokamak H-mode

Axes: $\log_{10}(\tau_{ISS04}$ (s)) versus $\log_{10}(\tau_E$ (s))

Lower-Mirror

a

T (keV)

T_e (TS)
T_e (ECE)
T_i (XICS)
T_e (Probe)

b

n (10^{19} m^{-3})

n_e (TS)
n_i

1.5

Z_{eff} = 2.5

3.5

Higher-Mirror

c

T (keV)

T_e (TS)
T_e (ECE)
T_i (XICS)
T_e (Probe)

r_{eff} (m)

d

n (10^{19} m^{-3})

n_e (TS)
n_i

1.5

Z_{eff} = 2.5

3.5

r_{eff} (m)

Lower-Mirror

a E_r (kVm^{-1}) vs r_{eff} (m)
- XICS
- NTSS

b P (MW) vs r_{eff} (m)
- $q_{tot} V'$
- $P_{ECRH} - P_{rad}$
- $q_{NC}^e V'$
- $q_{NC} V'$

c j_{bs} (kAm^{-2}) vs r_{eff} (m)
- NTSS
- SFINCS

Higher-Mirror

d E_r (kVm^{-1}) vs r_{eff} (m)
- Refl.
- XICS
- NTSS

e P (MW) vs r_{eff} (m)
- $q_{tot} V'$
- $P_{ECRH} - P_{rad}$
- $q_{NC}^e V'$
- $q_{NC} V'$

f j_{bs} (kAm^{-2}) vs r_{eff} (m)
- NTSS

Supplementary Information

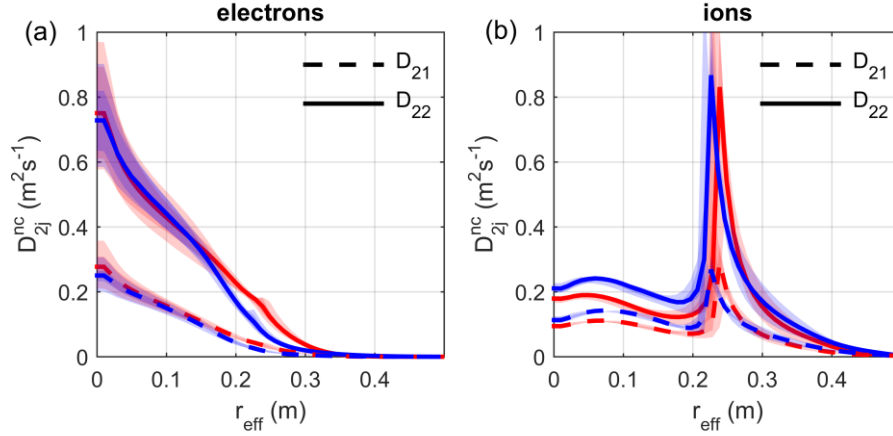# Neoclassical radial transport coefficients for W7-X limiter magnetic configurations and confinement data

C.D. Beidler, A. Dinklage, G. Fuchert

The normalized mono-energetic radial transport coefficients $D_{11}^{\star}$ for the 'lower-mirror' and 'higher mirror' magnetic configurations calculations with the DKES code at an effective radius of r_{eff} = 6cm are shown in Supplementary Fig. 1 (using the same terminology as in [35]: $v^{\star} = (\nu R/(\iota v))$ is the collisionality with the collision frequency ν the major radius R, the rotational transform ι and the particle velocity v).
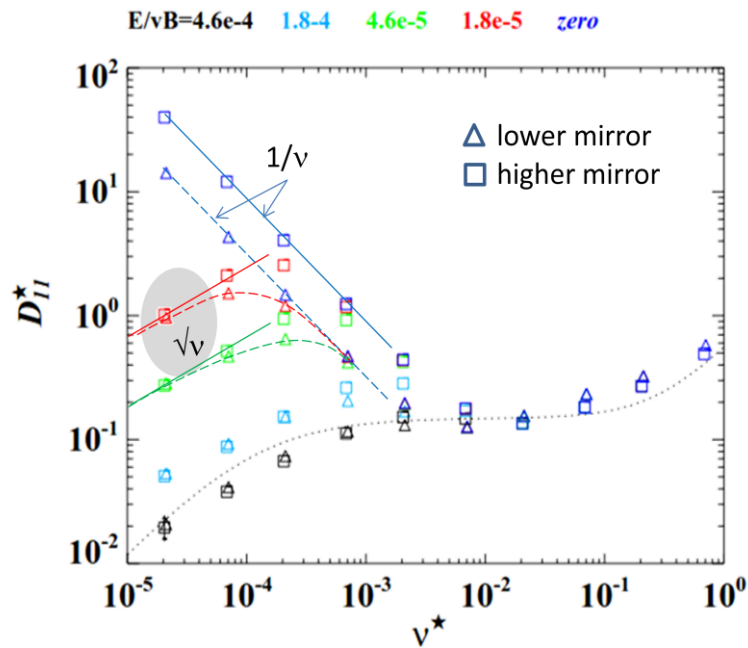
Supplementary Fig. 1| Normalized mono-energetic radial transport coefficient. The transport coefficients $D_{11}^{\star}$ are shown for the higher-mirror (squares) and lower-mirror (triangles) configurations as functions of collisionality and normalized radial electric field at a minor plasma radius of r_{eff} = 6cm. The portion of the plot making the largest contribution to the thermal neoclassical energy transport coefficient for the electrons (largest energy loss channel, see Fig. 6**b** and **e**) at experimental temperatures, densities and radial electric field (Figs. 5, 6**a,f**) is indicated by the gray shaded area.

Supplementary Fig. 1 shows minor differences for the $D_{11}^\star$ between the investigated magnetic configurations in the $\sqrt{\nu}$ regime at the collisionalities and electric field values relevant for the experimental conditions in this paper (indicated by the grey shaded area; in order to ease the identification of differences between the configurations, the solid and dashed lines are provided at fixed $E_r/\text{v}B$. Results for $1/\nu$ transport differ by roughly a factor of two, as the $E_r/\text{v}B = 0$ results indicate, but such small values of the electric field are of no relevance under electron-root conditions.

Supplementary Fig. 2| Thermal neoclassical energy transport coefficients. The plots show thermal energy transport coefficient profiles for electrons (**a**) and ions (**b**) for all plasma radii as used in NTSS (for the results shown in Fig. **5d** and **i**). Blue refers to the lower mirror case, red to the higher mirror case. The error band result from error propagation of the profile uncertainties.

Supplementary Fig. 2 shows the thermal transport coefficients as obtained by the energy convolution of $D_{11}^\star$ [35] for the temperatures, densities and radial electric field given at each radial position of the plasma:

$$D_{22}^{nc} = L_{22} - \frac{3}{2}L_{21}$$

$$D_{21}^{nc} = L_{21}$$

with (1) $L_{ij} = \frac{2}{\sqrt{\pi}}\int_0^\infty dK\sqrt{K}\exp(-K)\,D_{11}^\star(K)\,D_{11}^p h_i h_j,\ h_1 = 1, h_2 = K$

and $K = (m\text{v}^2/2)/T$ and $D_{11}^p = \pi/4\,(\text{v}_d^2\text{R})/(\text{v}t)$ the mono-energetic transport coefficient of the plateau regime (used in the normalization of $D_{11}^\star$). $\text{v}_d = m\text{v}^2/(2q\text{B}\text{R})$ is a radial drift velocity of

2

a particle with charge q. In order to estimate the range of K values which make the predominant contribution to transport (e.g. gray shaded area in Supplementary Fig. 1), the integrand of Eq. (1) is maximized. For energy transport this leads to largest contributions at K values well in excess of one.

The error bands reflect the influence of uncertainties in the profiles and Z_{eff} on the values of the thermal transport coefficients. In the core region ($E_r > 0$), the ion transport coefficients (Supplementary Fig. **2b**) are smaller than those of the electrons (Supplementary Fig. **2a**). At the same time, the gradients of the ions are also smaller than those of the electrons. Therefore, the ion contributions of the neoclassical energy fluxes are smaller than the dominating electron contributions (cf. Fig. **6b** and **e** in the main paper). The electron energy transport coefficients (Supplementary Fig. **2a**) match for both configurations (except for the small region of E_r/vB =0 in which $1/\nu$ transport is of relevance leading to larger transport coefficients in the higher-mirror case). Since also the plasma profiles are very similar (cf. Fig. 5), it can be concluded from the transport coefficients that the neoclassical contribution to the energy transport (Figs. 6**b** and **e**) is also very similar for the two magnetic configurations discussed in this paper. Since radiation and signals qualitatively indicating neutral particle fluxes are not different either, the similarity of neoclassical transport allows for the conclusion that also anomalous transport is not affected by the configuration change.

Supplementary Tab. 1 summarizes the W7-X confinement data shown in Fig. 4. The experimental confinement time was derived from the profiles as shown in Fig. 5. Uncertainties in the experimental confinement time τ_E include uncertainties in the profiles and Z_{eff}. The heating power and line averaged density correspond to the waveforms shown in Fig. 3 (with a chord length of L = 1.3 m). Errors in the mean density and the heating power are used to estimate the uncertainties of τ_{ISS04}.

Case	Heating power (MW)	Mean plasma density (m^{-3})	τ_E (ms)	τ_{ISS04} (ms)
*Lower mirror, higher power	1.07±0.11	0.91±0.09	122± 24	139±16
*Lower mirror, lower power	0.56±0.06	0.76±0.08	137± 27	187±23
$^+$Higher mirror, higher power	1.03±0.10	0.99±0.10	124± 25	151±17
$^+$Higher mirror, lower power	0.58±0.06	0.89±0.09	157± 31	203±24
*Best τ_E/ τ_{ISS04} (OP1.1)	3.80±0.38	2.73±0.27	128± 25	117±14

Supplementary Tab. 1| Energy confinement times in the first operation phase of W7-X.

Further scaling parameters for the configurations (*lower mirror, $^+$higher mirror) are summarized in Supplementary Tab. 2.

For the reference confinement time τ_{ISS04}, the ISS04 scaling expression [25].

$$\tau_{ISS04} = 0.134 a^{2.28} R^{0.64} P^{-0.61} n^{0.54} B^{0.84} t_{2/3}^{0.41}$$

was evaluated with the minor radius a, the major radius R, the mean magnetic field B and the rotational transform $t_{2/3}$ taken at 2/3 of the normalized plasma radius r_{eff}/a. Values of these parameters were calculated with VMEC calculations and are summarized in the supplementary Tab. 2. As for Ref. [25], uncertainties in the rotational transform minor radius and major radius are not considered. For the specific case discussed in the main article, the errors in the minor radius and the major radius is expected to be smaller than for other cases in the ISS04 database, since the plasma volume is well defined by limiters.

Case	rotational transform at 2/3 of the plasma radius $t_{2/3}$	Magnetic field B (T)	Minor radius a (m)	Major radius R (m)
*Lower mirror	0.814	2.414	0.491	5.514
+Higher mirror	0.843	2.365	0.497	5.488

Supplementary Tab. 2| Confinement time scaling parameters for W7-X limiter configurations. The specific values are results from VMEC calculations also used for coordinate transformations (cf. Methods section).